Materials Characterization 234 (2026) 116139

Contents lists available at ScienceDirect

Materials Characterization

journal homepage: www.elsevier.com/locate/matchar

Superlattice phase precipitation in Ti-Fe-Mo-Al alloys

A.M.L. Andersson, R.F.L. Mellor, J.M. Hogg, H.C. Cole, G.I. Lampronti, N.L. Church, O.S. Houghton, N.G. Jones, H.J. Stone *

Department of Materials Science and Metallurgy, University of Cambridge, 27 Charles Babbage Rd, Cambridge, CB3 0FS, UK

ARTICLE INFO

Keywords:
Ti alloys
Superlattice precipitation
A2+B2 phase equilibria
Discontinuous precipitation
Electron microscopy
Synchrotron X-ray diffraction

ABSTRACT

Ti-Fe-Al and Ti-Fe-Mo alloys containing B2 superlattice precipitates within an A2 matrix have attracted interest for structural applications. However, few studies have considered alloys derived from the quaternary Ti-Fe-Mo-Al system. In this work, six Ti-Fe-Mo-Al compositions with 70 at.% Ti have been aged for 1000 h at 600, 800, and 1000 °C to assess their equilibrium phases. A2+B2 phase microstructures formed in two of the alloys considered: Ti-20Fe-5Mo-5Al at both 800 and 1000 °C, and Ti-15Fe-10Mo-5Al at 800 °C. A2+B2 microstructures were not observed in the other alloys investigated. At high temperatures, most alloys were single-phase A2, while at lower temperatures A3 and $D0_{19}$ phases were widely observed.

Studying continuous cooling of Ti-20Fe-5Mo-5Al from the solid solution showed a change in precipitation behaviour with cooling rate. Intermediate cooling rates permitted discontinuous B2 precipitation. The slowest cooling rate led to continuous B2 precipitation and the observation of the $D8_a$ G-phase. This transition in precipitation mechanism was attributed to the relative rates of bulk and grain boundary diffusion at varying temperatures.

1. Introduction

Alloy microstructures comprising superlattice precipitates coherently embedded within a solid solution matrix are exploited within several classes of high-performance alloys for structural applications. Notable examples include Ni- and Co-based superalloys [1,2], Al-Sc [3,4], Al-Li [4,5], and Pt-Al [6] alloys. However, to date, no superlattice precipitate-strengthened Ti-based alloy has been commercialised.

Ti-rich alloys within the Ti-Fe system have previously been investigated as they can form a TiFe B2 phase within an A2 solid solution (Strukturbericht notation). The eutectic A2-B2 transformation at 29.5 at.% Fe and 1085 °C [7] has been utilised to form fine as-cast microstructures [8]. This has led to eutectic and hypoeutectic (25 at.% Fe) alloys showing impressive properties in the as-cast state, with high compressive 0.2% proof stress of around 1.85 GPa. An alternative approach to achieving A2+B2 microstructures is through solid-state precipitation from a single-phase solid-solution [9]. This can be achieved for binary alloys containing 14.8 to 20.9 at.% Fe [7]. Ageing of Ti-20Fe at 600 °C led to precipitation of the B2 phase, but also the formation of brittle A3 and ω phases, with ω significantly increasing hardness. Notably, the hardness of this alloy decreased upon ageing, which was attributed to a significant loss of solid solution strengthening [9].

Ternary additions to Ti-Fe alloys including Sn [8,10], Cu [8], Co [8], Mo [11–14], and Al [15–17] have been investigated to assess their impact on strength, ductility, lattice coherence, and microstructural stability. Mo has been of particular interest as it is a potent A2 phase stabiliser, suppressing transformation to the A3 phase [18] and decreasing ω phase formation [19]. In addition, it preferentially partitions to the A2 phase, and can therefore be used to modify lattice misfit between the A2 and B2 phases, impacting coherency [13]. Elevated Mo contents have also been shown to change the morphology of B2 precipitates, with Ti-20Fe-10Mo forming spherical B2 after a 750 °C age, while Ti-20Fe-20Mo and Ti-10Fe-40Mo formed lamellar B2 after the same ageing treatment, which increased hardness [13]. Recent studies have also shown that benefits may be derived from Al additions, which lead to nanostructuring of B2 precipitates that reduces lattice misfit and thereby improves precipitate-matrix coherence [15]. However, excessive concentrations of Al stabilise the A3 phase, potentially compromising the A2+B2 microstructure and leading to embrittlement [20].

While studies of alloys from the Ti-Fe-Mo and Ti-Fe-Al ternaries have identified benefits, little is known about A2+B2 phase equilibria in the Ti-Fe-Mo-Al quaternary. To gather information on the phase equilibria in this system, six compositions in the Ti-Fe-Al-Mo quaternary with 70 at.% Ti have been investigated. The composition with the

* Corresponding author.
E-mail address: hjs1002@cam.ac.uk (H.J. Stone).

https://doi.org/10.1016/j.matchar.2026.116139
Received 16 September 2025; Accepted 6 February 2026
Available online 2 March 2026

widest temperature range over which an A2+B2 microstructure is stable was identified, and the mechanisms through which B2 precipitates formed were studied.

2. Experimental

Predictions of thermodynamic equilibria in the Ti-Fe-Mo-Al system were made using Thermo-Calc 2022b [21] with the TCTI2 database. Calculations were performed for a series of compositions within the 70 at.% Ti pseudo-ternary in which the concentrations of Fe, Mo, and Al were varied in increments of 5 at.%. From these calculations, six alloy compositions were selected that were predicted to have A2+B2 phase equilibria at 800 °C. The nominal compositions of the selected alloys are given in Table 1. Ingots weighing approximately 40 g of each composition were made with constituent elements of >99.9% purity through arc melting in an Ar atmosphere. Each ingot was inverted and remelted three times to ensure compositional homogeneity. The bars were sectioned, encapsulated under Ar in a silica tube together with a Ta getter, and solution treated at 1115 °C in a box furnace for 50 h then water quenched. The temperature was measured to ±1 °C using an N-type thermocouple. Each bar was then sectioned into three pieces that were respectively aged at 600, 800 and 1000 °C for 100 h using the same protocol as the solution treatment.

An additional bar of nominal composition Ti-20Fe-5Mo-5Al at.% was arc melted as described above. Five 10 mm sections with parallel faces were cut from this bar, and 4 mm diameter cylinders were made using electro-discharge machining. These sections were solution treated in the same way as the previous samples, at 1115 °C for 50 h. The cylinders were subsequently individually heat treated using a DIL805 dilatometer (TA instruments) under vacuum (max 8×10^{-4} mbar) with a thermal cycle comprising heating from room temperature to 1115 °C at a rate of 10 °C s^{-1}, dwelling at 1115 °C for 5 min, and controlled linear cooling to room temperature at rates of 40 °C s^{-1}, 10 °C s^{-1}, 1 °C s^{-1}, 0.1 °C s^{-1}, or 0.01 °C s^{-1}.

Both the furnace-aged samples and the samples that had undergone controlled cooling were mounted in conductive bakelite, mechanically ground to a 4000 grit finish using SiC abrasive papers, and polished using buffered OPUS (0.04 μm colloidal silica). Microstructural images of the samples were acquired by scanning electron microscopy (SEM) using the back-scattered electron (BSE) signal in a Zeiss GeminiSEM 300 and a Hitachi TM4000Plus. The former microscope was used together with an Oxford Instruments X-Max^N 50 detector for compositional analysis through energy dispersive X-ray spectroscopy (EDX). A working distance of approximately 5 mm, an aperture of 30 μm, and an accelerating voltage of 25 keV were used in the Zeiss microscope, while a working distance of 8 mm and an accelerating voltage of 15 keV were used in the Hitachi microscope. Any compositional data reported is an average of a minimum of five separate sites, with bulk compositions being the average over five approximately 500×500 μm^2 areas.

Slices of the furnace-aged samples, approximately 1 mm thick, were prepared for X-ray diffraction (XRD) by mechanical grinding to a 1200 grit finish. XRD data were acquired using a Bruker D8 Advance diffractometer equipped with Ni-filtered Cu K-α radiation, a LynxEye EX position sensitive detector with ~ 6.5% energy resolution and variable divergence slits. Scans were taken over 20 to 130° 2θ using an 8 mm illumination length, with 0.035° step size and 2 s dwell time per step.

Synchrotron XRD (sXRD) diffraction data were acquired from the controlled linear cooling samples using the ID22 high-resolution powder diffraction beamline at the European Synchrotron Radiation Facility (ESRF), Grenoble, France, under experiment MA-5868. Samples for these measurements were ground to a powder using a pestle and mortar and placed in individual silica tubes that were spun at 991 revolutions per minute. The incident monochromatic beam was determined to have a wavelength of 0.354273 ± 0.000 004 Å using a silicon NIST standard. The beam cross-section was 2×1 mm^2 and the diffraction patterns were collected using a 13-channel Si 111 multi-analyser stage between the sample and a Dectris Eiger2 X 2M-W CdTe pixel detector with individual detectors separated by 2° in 2θ. For each sample, three scans were performed with the central detector ranging from 0° to 30° at a scan speed of 5 ° min^{-1}. Each set of three scans was averaged, and Rietveld refinements [22] were performed using Pearson VII peak profiles in Topas-Academic-64 V6 and jEdit version 4.3.1. Crystallographic Information Files (CIF) for each of the constituent phases were obtained from the Inorganic Crystal Structure Database (ICSD ©FIZ Karlsruhe GmbH) and copies are given in the supplementary information S1.

Table 1
Nominal compositions of the six alloys investigated in this study, along with their average measured compositions determined by EDX (in at.%). Quoted uncertainties are the standard deviation of five measured values.

	Ti	Fe	Mo	Al
Nominal composition	70	20	5	5
Measured composition	72.0 ± 0.2	19.9 ± 0.3	3.2 ± 0.1	5.0 ± 0.1
Nominal composition	70	15	10	5
Measured composition	71.5 ± 0.2	14.8 ± 0.2	8.5 ± 0.2	5.1 ± 0.1
Nominal composition	70	15	5	10
Measured composition	71.7 ± 0.2	14.6 ± 0.4	3.6 ± 0.3	10.2 ± 0.2
Nominal composition	70	10	15	5
Measured composition	71.0 ± 0.2	10.0 ± 0.3	14.1 ± 0.7	5.0 ± 0.4
Nominal composition	70	10	10	10
Measured composition	71.1 ± 0.6	9.8 ± 0.3	9.1 ± 0.3	10.0 ± 0.7
Nominal composition	70	10	5	15
Measured composition	71.5 ± 0.3	9.9 ± 0.3	4.1 ± 0.1	14.5 ± 0.2

An electron-transparent foil of Ti-20Fe-5Mo-5Al cooled at 0.1 °C s^{-1} was produced using focused-ion beam (FIB) milling in a FIB/SEM FEI Helios Nanolab microscope. This was representative of the interface region between the two microstructural types in the sample. An FEI Tecnai Osiris 80-200 operated at an accelerating voltage of 200 keV was used for transmission electron microscopy (TEM), scanning transmission electron microscopy (STEM), STEM-EDX, and high-angle annular dark field (HAADF) imaging. Selected area diffraction patterns (SADP) were acquired using a Gatan OneView UltraScan camera. STEM data were processed using version 2.0.1 of the Hyper-Spy Python package.

Vicker's hardness data were obtained using a Qness Q30 A+ automatic hardness tester with a 5 kg load. The hardness values quoted are the average and standard deviation of five indents in mounted, polished sections from the samples subjected to controlled cooling.

3. Results

3.1. Equilibrium phase determination

The nominal compositions of the six investigated alloys and the compositions measured by EDX are given in Table 1. The concentrations of Fe and Al achieved in the alloys were close to the nominal values, however, Mo inclusions from incomplete melting during the production led to Mo depletion in the bulk of the sample in the range of 0.9-1.9 at.%. These discrepancies were considered acceptable for the purposes of the study. Pseudoternary phase diagrams of Ti-Fe-Mo-Al with 70 at.% Ti at 600, 800, and 1000 °C, predicted using Thermo-Calc, are shown in Fig. 1. Markers corresponding to the measured compositions projected onto the 70 at.% Ti pseudoternary are included for reference.

A representative XRD pattern from Ti-10Fe-5Mo-15Al after ageing at 800 °C for 1000 h is given in Fig. 2. The XRD patterns for the other compositions and ageing temperatures are available in the supplementary information S2. Reflections corresponding to A2, B2, and $D0_{19}$ (Ti_3Al) phases have been identified and labelled. While the A3 and $D0_{19}$ phases have several common peaks, the $D0_{19}$ phases can be unambiguously identified through the occurrence of unique superlattice

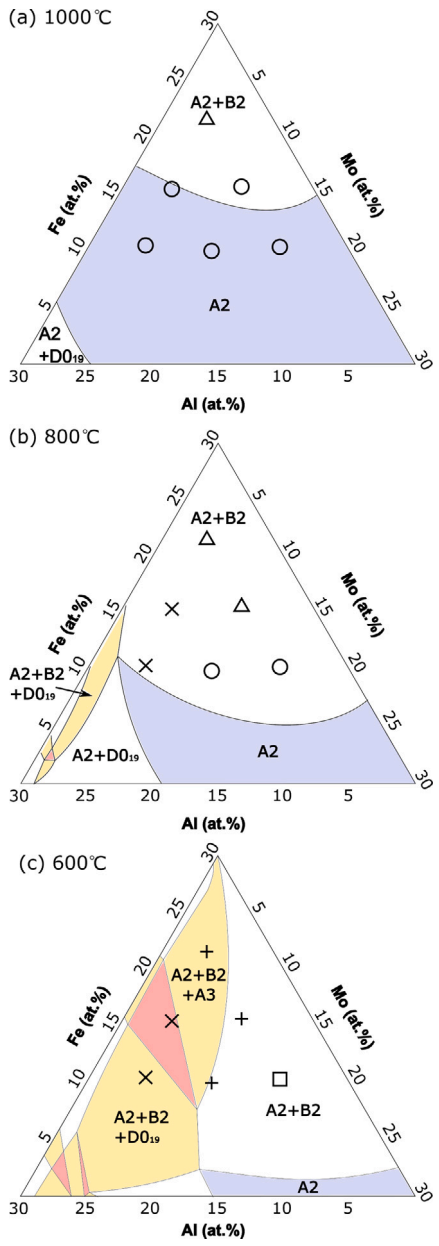

Fig. 1. Pseudo-ternary 70Ti-Fe-Mo-Al phase diagrams for (a) 1000 °C, (b) 800 °C, and (c) 600 °C as predicted by Thermo-Calc [21]. The position of markers corresponds to the nominal investigated compositions, and their shape corresponds to the phases observed in XRD.

reflections such as {210}. However, as these are low-intensity reflections, the inability to identify specific superlattice peaks in addition to the fundamental reflections does not exclude the possibility of the $D0_{19}$ phase being present. For this reason, in alloys where distinct peaks from the $D0_{19}$ phase could not be discerned, these phases were classified as A3/$D0_{19}$. The phases identified in each sample using XRD are indicated in Fig. 1 by use of different-shaped markers. A circle indicates single-phase A2. A triangle indicates two-phase A2+B2. A cross indicates A2+B2+$D0_{19}$, as superlattice reflections were identified. A plus-sign indicates A2+B2+A3/$D0_{19}$, as no superlattice reflections were identified. Finally, a square shows A2+A3/$D0_{19}$ were identified, with no B2 reflections.

The SEM-BSE images in Figs. 3, 4, and 5 show the microstructures of the six alloys after ageing at 1000, 800 and 600 °C for 1000 h, respectively. After ageing at 1000 °C, all alloys except Ti-20Fe-5Mo-5Al exhibited single-phase microstructures along with XRD patterns consistent with an A2 phase, seen in Fig. 3. This suggests these compositions reside in a single-phase field at this temperature. Ti-20Fe-5Mo-5Al exhibited large, blocky intraganular precipitiates and smaller, spheroidal precipitates in the A2 matrix. EDX point analyses indicated both precipitate types were consistent, with a composition of 53.1 ± 0.9% Ti, 43.8 ± 1.1% Fe, 0.9 ± 0.1% Mo, 2.2 ± 0.1% Al (at.%), consistent with that expected of the B2 TiFe phase. This phase identification is supported by the XRD data, which showed discernible A2 and B2 phase reflections.

The microstructures following ageing at 800 °C for 1000 h are shown in Fig. 4. The Ti-20Fe-5Mo-5Al alloy microstructure contained a bimodal distribution of light-contrast precipitates in an A2 matrix. The composition of the precipitates was 49 ± 2% Ti, 48 ± 3% Fe, 1.3 ± 0.8% Mo, 0.8 ± 0.2% Al (at.%) according to EDX point analysis. Together with the XRD pattern containing A2 and B2 reflections, this suggests that these precipitates are the B2 phase. The Ti-15Fe-10Mo-5Al alloy microstructure contained dendritic and blocky precipitates with a dark contrast in an A2 matrix. The measured composition was 54.7 ± 1.4% Ti, 41 ± 2% Fe, 2.5 ± 0.6% Mo, 1.8 ± 0.2% Al (at.%), which is again consistent with the B2 TiFe phase and supported by the occurrence of B2 reflections in the XRD data. The inversion in contrast between the matrices and precipitates in Ti-20Fe-5Mo-5Al (Fig. 4a) and Ti-15Fe-10Mo-5Al (Fig. 4b) can be attributed to the higher Mo content in the matrix of the latter alloy, increasing the atomic number contrast of the matrix relative to the precipitates. Alloy Ti-15Fe-5Mo-10Al contained light-contrast precipitates in an A2 matrix, which were similarly identified as B2 using EDX point analysis and XRD. It additionally contained a dark-contrast phase enriched in Al, with composition 74 ± 3% Ti, 5 ± 3% Fe, 1.0 ± 0.7% Mo, 19.9 ± 1.3% Al (at.%). This composition is consistent with the $D0_{19}$ Ti_3Al phase, which was identified in the XRD pattern, suggesting this alloy lies in a three-phase field at this temperature. Contrastingly, alloys Ti-10Fe-15Mo-5Al and Ti-10Fe-10Mo-10Al appear to lie in a single-phase A2 field, according to their microstructure and the XRD results. The final investigated composition, Ti-10Fe-5Mo-15Al, contained light and dark contrast precipitates in an A2 matrix, which were identified as B2 and $D0_{19}$ phases, respectively, using point EDX and XRD data.

After ageing at 600 °C for 1000 h, significant fine-scale precipitation was observed in most alloys within an A2 matrix, seen in Fig. 5. No EDX compositional analyses were performed on the precipitates as the EDX interaction volume was expected to be larger than the particle size. However, the consistency in the XRD data and BSE phase contrast of the 600 °C aged samples with the 800 °C aged samples suggests the precipitates were the A3/$D0_{19}$ and B2 phases. Ti-20Fe-5Mo-5Al contained fine dispersions of dark A3/$D0_{19}$ and light B2 precipitates within an A2 matrix. Regions of radial-type precipitate growth were also observed. Ti-15Fe-10Mo-5Al contained light-contrast B2 phase that was present in two distinct morphologies that were well separated: lamellar colonies and spheroidal precipitates. Isolated occurrences of the dark-contrast $D0_{19}$ phase were additionally observed. Ti-15Fe-5Mo-10Al contained intergrowths of the $D0_{19}$, B2, and A2 phases that had a feathery appearance. A similar microstructure was observed in alloy Ti-10Fe-5Mo-15Al. In contrast, the microstructure of Ti-10Fe-15Mo-5Al was dominated by the A2 phase. Fine light and dark-contrast precipitates were observed on grain boundaries. While reflections corresponding to the A3/$D0_{19}$ phases could be identified in the XRD data, no B2 reflections were seen, possibly due to the small volume fraction observed in the microstructure. Finally, in the Ti-10Fe-10Mo-10Al alloy, a matrix of A2 containing dark-contrast A3/$D0_{19}$ precipitates was observed. In addition to these phases, the XRD data contained reflections corresponding to the B2 phase. However, distinct B2 precipitates were not found during microstructural examination.

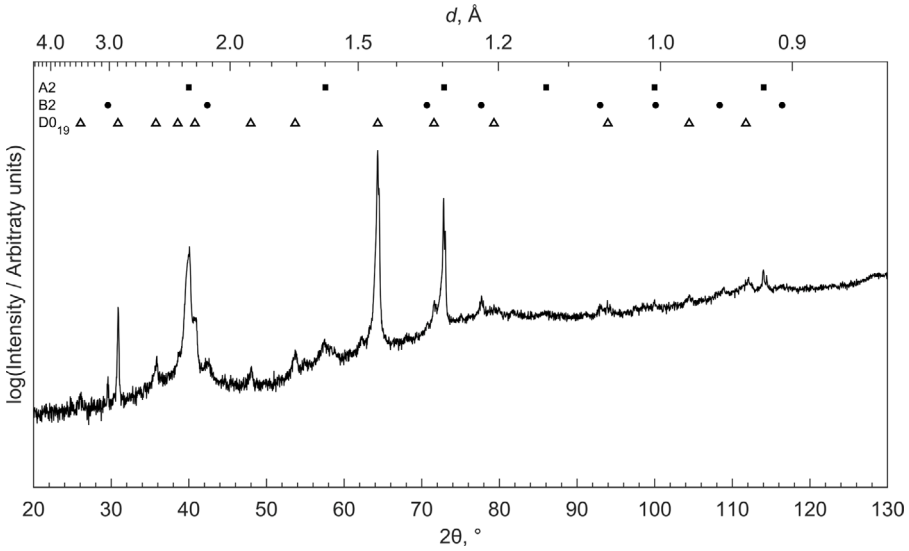

Fig. 2. Ti-10Fe-5Mo-15Al XRD pattern after 1000 h at 800 °C. Reflections from A2, B2, and $D0_{19}$ phases are seen, including a $D0_{19}$ superlattice reflection at 49°.

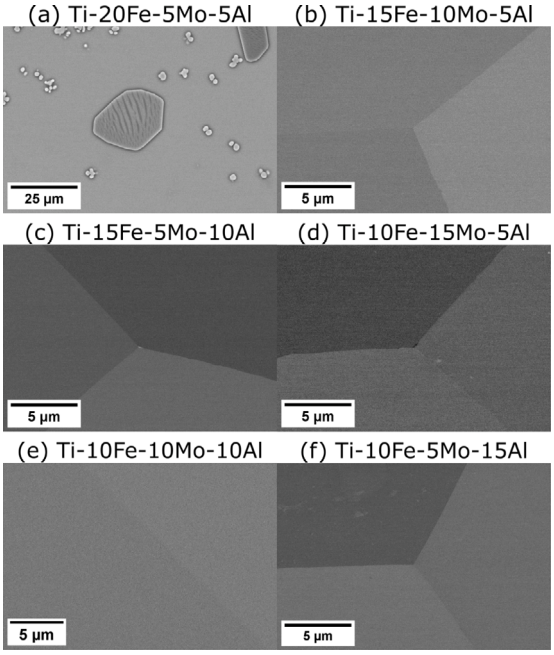

Fig. 3. SEM-BSE images after ageing at 1000 °C for 1000 h for (a) Ti-20Fe-5Mo-5Al, (b) Ti-15Fe-10Mo-5Al, (c) Ti-15Fe-5Mo-10Al, (d) Ti-10Fe-15Mo-5Al, (e) Ti-10Fe-10Mo-10Al, (f) Ti-10Fe-5Mo-15Al. Note the scale difference for (a), used to show the B2 precipitates present.

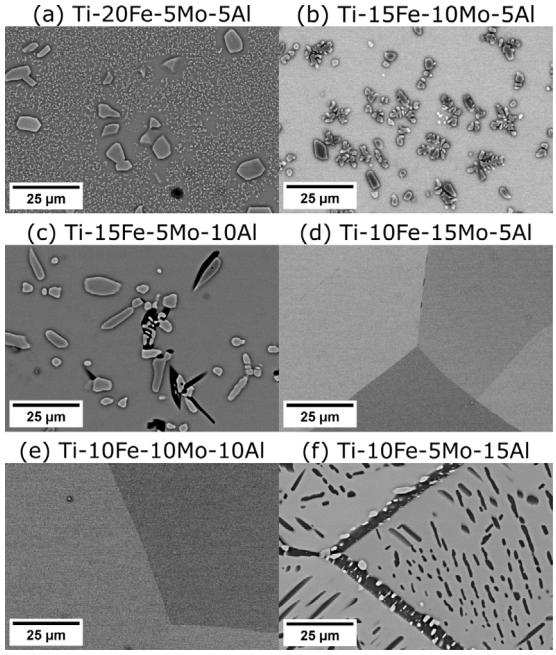

Fig. 4. SEM-BSE images of samples aged at 800 °C for 1000 h for (a) Ti-20Fe-5Mo-5Al, (b) Ti-15Fe-10Mo-5Al, (c) Ti-15Fe-5Mo-10Al, (d) Ti-10Fe-15Mo-5Al, (e) Ti-10Fe-10Mo-10Al, (f) Ti-10Fe-5Mo-15Al.

3.2. Microstructural dependence on cooling rate

Ti-20Fe-5Mo-5Al was the only composition to form an A2+B2 microstructure at both 1000 °C and 800 °C, suggesting it had the most extensive A2+B2 phase field of the alloys studied. In addition, the observation of a bimodal B2 precipitate distribution in this alloy after ageing at 800 °C suggests that B2 precipitation may have occurred during the water quench. Given the rapid cooling rates associated with water quenching, this warranted further examination of the microstructural dependence on cooling rate. Therefore, a series of controlled cooling rate experiments was carried out on this alloy. Fig. 6 shows the microstructure of the samples cooled from 1115 °C at linear rates ranging from 40 °C s^{-1} to 0.01 °C s^{-1}.

The fastest cooling rate, 40 °C s^{-1}, led to an apparent single-phase microstructure. At 10 °C s^{-1} and 1 °C s^{-1}, partial transformation of the matrix to a lamellar two-phase structure occurred. This lamellar transformation originated at grain boundaries, implying a discontinuous precipitation (DP) mechanism. Cooling at 0.1 °C s^{-1} led to a dual microstructure, with regions containing spheroidal precipitates formed through a continuous precipitation (CP) mechanism, separated by lamellar DP colonies. After the slowest cooling at 0.01 °C s^{-1}, all precipitates were blocky or spheroidal, indicating only CP occurred.

To confirm the identity of the phases formed through DP and CP, a FIB foil from the region across the boundary between the two

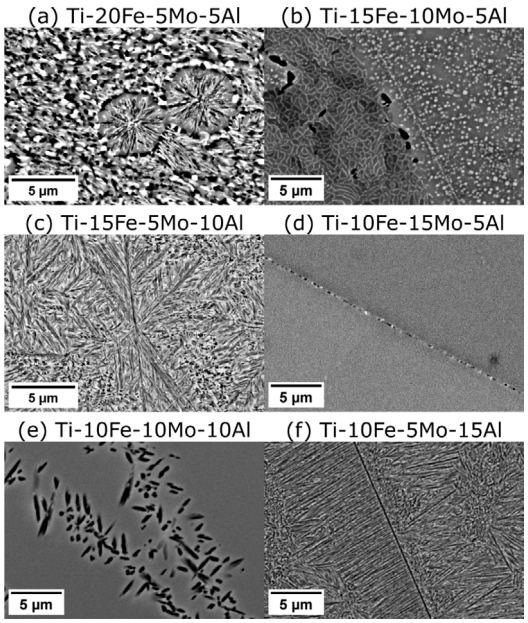

Fig. 5. SEM-BSE images after ageing at 600 °C for 1000 h for (a) Ti-20Fe-5Mo-5Al, (b) Ti-15Fe-10Mo-5Al, (c) Ti-15Fe-5Mo-10Al, (d) Ti-10Fe-15Mo-5Al, (e) Ti-10Fe-10Mo-10Al, (f) Ti-10Fe-5Mo-15Al.

morphologies in the 0.1 °C s^{-1} cooled sample was investigated using TEM. Fig. 7 shows a HAADF image and STEM-EDX maps of the same region. The precipitates in the continuous region and the bright-contrast lamella in the discontinuous region were enriched in Fe and depleted in Ti, Mo, and Al, as would be expected of the TiFe B2 phase. The similar compositional variation in both regions suggests the same phase is being formed through different mechanisms.

SADPs taken down the [100] axis in the DP region and down [110] in the CP region are shown in Fig. 8 along with their associated key diagrams. Both SADPs show A2 reflections and fundamental B2 reflections slightly offset due to a difference in lattice parameters. Weak, diffuse streaks in the [110] pattern surrounding the superlattice reflections were observed.

All controlled cooling samples were examined using sXRD to confirm the identity of the phases present and to quantify their volume fractions and lattice parameters. The sXRD patterns with labelled peaks are shown in Fig. 9, and the parameters obtained from full Rietveld refinements are included in the supplementary information S3. Volume fractions and lattice parameters of the identified phases are given in Table 2. Cooling at 40 °C s^{-1} led to near-single-phase A2, with 0.2% B2. The sharpness of the B2 peaks suggests large precipitates, which is unlikely given the small volume fraction and BSE images, hence, this may be contamination from the powder-making process. The sample cooled at 10 °C s^{-1} was also predominantly A2, with 0.3% B2. This is less likely to be contamination, given the peaks are broader and DP was observed in SEM-BSE images of the microstructure. The sXRD pattern for the 1 °C s^{-1} cooled sample showed two sets of A2 peaks in addition to the B2 peaks. This is further evidence of DP, as the two distinct lattice parameters correspond to the original A2 phase and the discontinuously transformed A2 phase. The boundary between prior A2 and the DP A2 is discontinuous in composition, resulting in two distinct lattice parameters. With CP, the composition would be expected to vary continuously in the matrix. This would result in a progressive variation in the lattice parameter, leading to one set of broadened peaks rather than the two distinct sets of sharp peaks observed.

Cooling at 0.1 °C s^{-1} also led to a set of B2 peaks and two distinct sets of A2 peaks, suggesting that the discontinuous transformation was incomplete. There are also two additional, low-intensity peaks. These

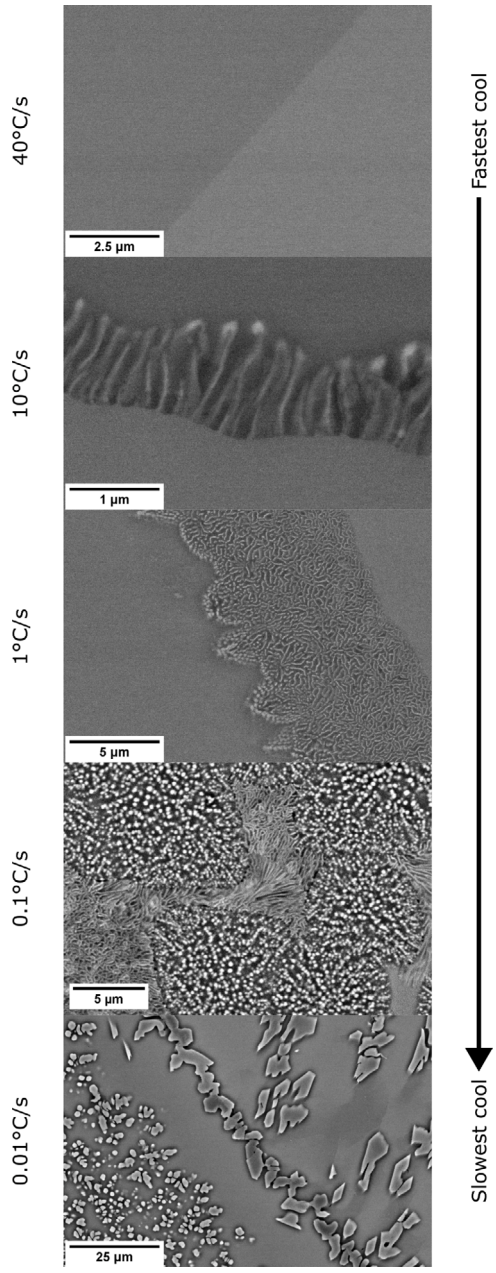

Fig. 6. SEM-BSE images of Ti-20Fe-5Mo-5Al linearly cooled from 1115 °C to room temperature at varying cooling rates. The precipitation goes from inhibited, to discontinuous, to continuous as the rate is decreased. Note the variation in scale to highlight microstructural features.

were also observed in the sXRD pattern from the 0.01 °C s^{-1} sample, where they were attributed to the presence of the $D8_a$ G-phase, also known as the τ_2 phase in the Ti-Al-Fe ternary system. Over the range of diffraction data acquired, 44 peaks could be assigned to the $D8_a$ phase, including the expected high-intensity peaks. This phase was not seen in the Ti-20Fe-5Mo-5Al samples aged at 600, 800, or 1000 °C, although the $D0_{19}$ phase was seen at 600 °C but not in any of the controlled cooling rate samples.

The hardness of the 40 °C s^{-1}, 10 °C s^{-1}, 1 °C s^{-1}, 0.1 °C s^{-1} and 0.01 °C s^{-1} cooled samples were HV549 ± 2, HV543 ± 6, HV534 ± 11,

Table 2
Phases present, volume fractions, and lattice parameters in Ti-20Fe-5Mo-5Al after cooling from 1115 °C at different rates, as determined from Rietveld refinements of the synchrotron data in Fig. 9. The 0.2% B2 present after the 40 °C s^{-1} cooling is suspected to be due to contamination.

Cooling rate	Phase	Volume fraction	Lattice parameter, ± 0.01 Å
40 °C s^{-1}	A2	99.92 ± 0.02%	3.15
	B2	0.08 ± 0.02%	3.02
10 °C s^{-1}	A2	99.79 ± 0.02%	3.15
	B2	0.21 ± 0.02%	2.99
1 °C s^{-1}	Original A2	88.837 ± 0.002%	3.15
	Transformed A2	8.319 ± 0.002%	3.20
	B2	2.844 ± 0.001%	3.00
0.1 °C s^{-1}	Original A2	24.200 ± 0.007%	3.15
	Transformed A2	66.00 ± 0.02%	3.20
	B2	9.659 ± 0.003%	3.00
	$D8_a$	0.15 ± 0.03%	11.34
0.01 °C s^{-1}	A2	73.1 ± 0.2%	3.20
	B2	18.4 ± 0.1%	3.00
	$D8_a$	8.5 ± 0.2%	11.34

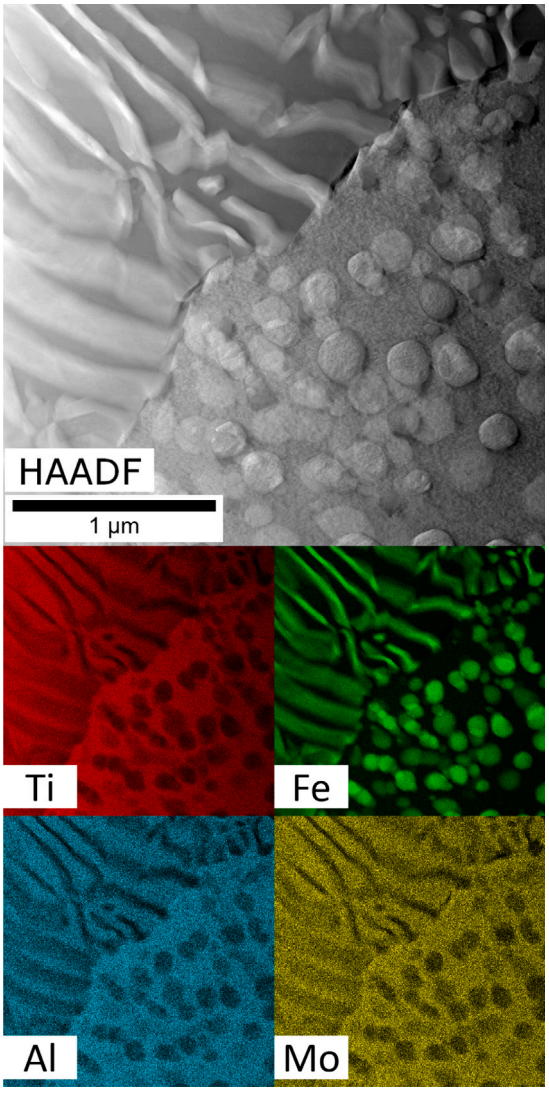

Fig. 7. HAADF and STEM-EDX of Ti-20Fe-5Mo-5Al after controlled cooling at 40 °C s^{-1} from 1115 °C, showing both lamellar, discontinuous precipitation and spheroidal, continuous precipitation. The spheroidal precipitates and one type of lamella are enriched in Fe and poor in Ti, Mo, and Al, as would be expected of B2 TiFe.

HV551 ± 9, and HV461 ± 3, respectively. The hardness was therefore the same within error for all samples except the 0.01 °C s^{-1} cooled sample, which was 15% lower.

4. Discussion

4.1. Phase equilibria

Ti-20Fe-5Mo-5Al was the only composition that exhibited an A2+B2 microstructure at two different tested temperatures, 1000 °C and 800 °C. It was also notable that fewer of the alloy compositions formed A2+B2 microstructures than predicted at all the temperatures considered. This suggests that the two-phase A2+B2 region is less extensive than predicted, with the single-phase A2 field extending to higher Fe contents and the three-phase A3/$D0_{19}$+B2+A2 phase fields extending to lower Al contents. This is especially prominent at 800 °C, at which only two compositions formed A2+B2 microstructures even though all six were predicted to do so.

While the $D0_{19}$ phase was seen after ageing at 600 °C for 1000 h in the Ti-20Fe-5Mo-5Al alloy, it was not observed in the sXRD patterns of the controlled cooling rate samples. Instead, the ternary G-phase ($D8_a$) based on Al_2FeTi was seen after the slowest cooling of 0.01 °C s^{-1}. In the works by Palm & Inden [23], Palm & Lacaze [16], and Gorzel et al. [17] this phase is only seen in the Ti-Fe-Al ternary system for compositions containing >15 at.% Al. It was therefore unexpected to observe this phase in Ti-20Fe-5Mo-5Al, which only contains 5 at.% Al. There are a few potential explanations for the discrepancy. First, the phase diagrams in the aforementioned studies [16,17,23] are for temperatures of 1000, 900, and 800 °C. These show a progressive increase in the $D8_a$ phase field with lower temperature. It is therefore possible that the slowest cooling rate used here provided sufficient time at temperatures below those of the phase diagrams, where the regions containing $D8_a$ potentially extend to lower AL compositions, permitting the phase to form. This may be aided by the presence of Mo in the alloy in this study, which is known to destabilise the B2 TiFe phase [12] and may therefore permit the $D8_a$ phase to exist in equilibrium with the other phases observed. However, as the $D8_a$ phase was not observed in the isothermally aged samples, its stable temperature range must be limited to below the lowest investigated temperature of 600 °C. Second, the formation of the $D8_a$ phase could arise as a result of Al accumulation at the A2/B2 interface. As the temperature is decreased, the volume fraction of B2 phase increases and the equilibrium Fe concentration in this phase rises [7]. This requires expulsion of Al from the precipitates, potentially locally increasing Al concentration to a level where $D8_a$ could form. This hypothesis is supported by the SEM-BSE observations, as the Al-rich, dark phase was only seen at the A2/B2 interface. However, no significant Al concentration increase at the interface was

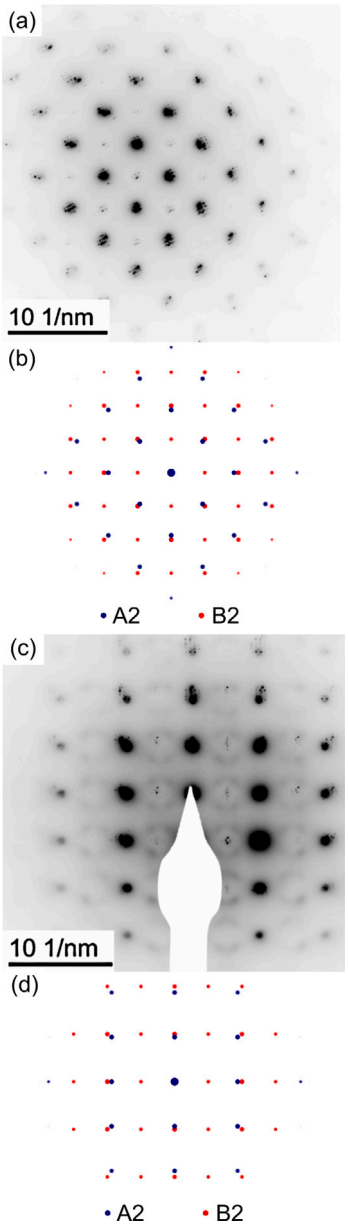

Fig. 8. Selected area diffraction patterns of Ti-20Fe-5Mo-5Al after controlled cooling at $40\,^{\circ}C\,s^{-1}$ from 1115 °C taken (a) down the [100] axis in a region with discontinuous B2 phase precipitates in an A2 phase matrix, (c) down the [110] axis in a region with continuous B2 phase precipitates in an A2 phase matrix. The respective key diagrams are in (b) and (d).

observed in the STEM-EDX data of the sample cooled at a faster rate of $0.1\,^{\circ}C\,s^{-1}$. If the Al accumulation after cooling at $0.01\,^{\circ}C\,s^{-1}$ was significant enough to allow for the $D8_a$ phase to be stable, it would have been reasonable to expect some degree of Al accumulation in the faster cooled sample. Third and finally, it is possible that the precipitation of $D0_{19}$ may be kinetically hindered during cooling. If a longer time close to the $D0_{19}$ solvus is required than is possible during the controlled cooling, the $D8_a$ phase could be formed in a metastable manner to counter the Al supersaturation in the A2 matrix at low temperatures. However, insufficient data have been acquired in the present study to conclusively determine the origin of the $D8_a$ phase.

It was notable that none of the precipitate populations in the tested alloys exhibited the plate-shaped morphology expected from

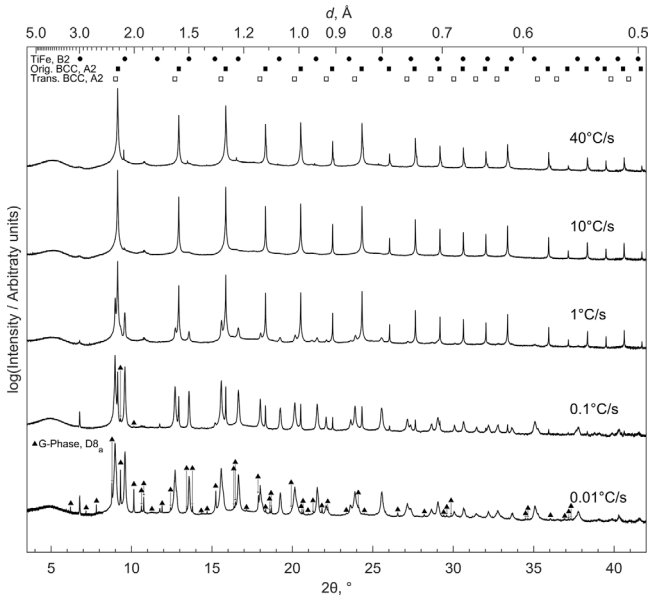

Fig. 9. Synchrotron data for Ti-20Fe-5Mo-5Al after linear, controlled cooling at various rates from 1115 °C. After the two fastest cools, $40\,^{\circ}C\,s^{-1}$ and $10\,^{\circ}C\,s^{-1}$, one set of A2 peaks is present, at $1\,^{\circ}C\,s^{-1}$ and $0.1\,^{\circ}C\,s^{-1}$ two A2 sets and a B2 set are present, and after the slowest cool, $0.01\,^{\circ}C\,s^{-1}$, one set of A2, B2 and $D8_a$ peaks are present.

nanostructuring and the occurrence of intra-precipitate orthorhombic phases [15]. This may be attributed to the increased stability of the A2 matrix achieved with the addition of Mo in the alloys investigated in the present study.

4.2. *Diffuse scattering from Ti-20Fe-5Mo-Al cooled at* $0.1\,^{\circ}C\,s^{-1}$

The diffuse spots/streaks in the [110] SADP of the CP region from the Ti-20Fe-5Mo-Al alloy cooled at $0.1\,^{\circ}C\,s^{-1}$ may arise from several different phenomena. First, athermal, incommensurate ω has been seen to produce spots at similar positions in SADPs acquired from other Ti alloys [24,25], including Ti-Fe binary alloys [9,26], although the spots that were reported were more clearly defined than those observed in this study. The ω could be identified as athermal and incommensurate using the construction presented by Nosonova et al. [26]. However, no ω reflections were observed in the sXRD pattern, so if present, this phase is either in a small volume fraction or sufficiently fine for Scherrer broadening to obscure the peaks within the background noise. As both Fe and Mo stabilise A2 Ti against ω formation [19], it is reasonable to expect a low volume fraction of fine ω, if present. Second, the diffuse scattering may be circular strain reflections due to strained coherent spherical superlattice precipitates [27]. As the SADP was taken in a continuously precipitated region that contained spherical B2 with a cube-cube orientation with the A2 matrix, a strained coherent interface could lead to halos around the superlattice reflections. However, the apertures in these circular halos should align towards the fundamental (000), which is not observed in this SADP.

4.3. *Effect of cooling rate on precipitation mechanisms*

As seen in Fig. 6, faster cooling of Ti-20Fe-5Mo-5Al promoted discontinuous precipitation, while slower cooling promoted continuous precipitation. Factors influencing the competition between these two precipitation mechanisms have been identified in several systems, such as Mg-Al [28,29], Al-Mg-Sc-Zr [30], and Ni superalloys [31,32], as well as through more general mathematical models [33,34]. These factors include the driving force for precipitation in the form of undercooling

and supersaturation, the relative rate of bulk and grain boundary diffusion, and grain boundary mobility. The interaction of these factors tends to give four temperature regimes with differing precipitation behaviour. However, as shown in the Mg-Al morphology map by Duly et al. [28], the exact temperatures at which each regime occurs may vary greatly with composition.

- *High temperature regime* - At high temperatures, DP mainly nucleates via the Fournelle & Clarke (F&C) mechanism [35]. This requires the pinning of thermally vibrating grain boundaries, which ceases above a critical temperature due to the high vibrational frequency [29]. The high bulk diffusion rate instead favours CP [28].
- *Intermediate temperature regime* - The nucleation rate of DP is highest immediately below the critical F&C temperature [28]. Additionally, the grain boundary mobility and grain boundary diffusion are high, permitting rapid DP growth [30]. In contrast, bulk diffusion is reduced, so the CP nucleation and growth rates are limited [34].
- *Low temperature regime* - A significant decrease in grain boundary mobility inhibits DP growth [30]. If bulk diffusion rates remain sufficiently high, some continuous precipitation can occur [28, 30].
- *Lowest temperature regime* - Diffusion and grain boundary movement, both thermally activated processes, are inhibited and no precipitation is seen.

In the cooling of Ti-20Fe-5Mo-5Al at variable rates, all of these regimes could be accessed, but the time spent in each depends on the cooling rate. Both mechanisms are strongly time dependent, so for CP to become prominent, some time needs to be spent in the high-temperature regime or a prolonged time in the low-temperature regime.

After cooling at the slowest rate of $0.01\,°C\,s^{-1}$, the B2 phase was observed to have only formed via CP. This indicates that the sample spent enough time in the high-temperature regime to fully undergo CP, similar to that seen in Mg-Al [29]. As no DP was observed, it may be concluded that there was insufficient supersaturation of Fe to provide a driving force for additional DP in the intermediate temperature regime [34].

After faster cooling at 1 to $10\,°C\,s^{-1}$, partial transformation of the matrix to DP A2+B2 was observed. This suggests that the time spent in the high-temperature regime was too short for the bulk diffusion needed for CP to occur. Instead, the supersaturation of Fe remained high until the intermediate-temperature regime was reached, and a DP transformation could occur. As DP growth occurs with a linear rate [30], the longer time spent in the intermediate temperature regime by the $1\,°C\,s^{-1}$ sample led to a greater fraction of the matrix having undergone a DP transformation than the $10\,°C\,s^{-1}$ sample.

Following the fastest cooling of $40\,°C\,s^{-1}$, a single-phase A2 microstructure was observed. This may be attributed to the sample not having spent enough time in any of the first three temperature regimes for precipitation to take place. The lack of CP at the fastest cooling rate is different from that observed in Al-Mg-Sc-Zr [30], indicating that the low temperature CP regime described may not exist in the Ti-Fe-Mo-Al system. Possible causes include an increased grain boundary mobility extending the intermediate-temperature DP regime to lower temperature, and the presence of slow-diffusing Mo, limiting bulk diffusion, therefore raising the limiting temperature at which all precipitation is inhibited. Together, these factors may allow for DP to dominate until precipitation is fully suppressed in the lowest temperature regime.

Cooling Ti-20Fe-5Mo-5Al at $0.1\,°C\,s^{-1}$ led to a combined CP and DP microstructure. This included spheroidal regions of CP, with larger precipitates in the centre of the region, and Dp lamellae surrounding the CP regions. This can qualitatively be understood in terms of the model presented by Robson [34]. In this sample, some CP occurred in the high-temperature regime, likely in regions with a small accumulation of Fe. Similar microsegregation has been observed in other A2 Ti alloys, causing β-flecking [36]. The increased supersaturation may then have led to a higher driving force for CP, and thus the precipitates formed during the limited time spent in the high-temperature regime. The highest Fe accumulation, in the centre of the region, would have led to CP at the highest temperature and thus allowed the longest time for coarsening. However, CP could not occur in regions without this increased driving force in this time frame, so both a supersaturated A2 matrix and continuous A2+B2 regions were present when the sample entered the intermediate temperature regime. For DP to occur, there must be a significant driving force for the breakdown of the supersaturated matrix, but when the moving grain boundary encounters a region of prior CP the supersaturation of Fe in the matrix is significantly lower. This decreases the driving force for DP growth to the extent that it does not occur in these CP regions, instead growing around them. This qualitatively follows the conclusion from Robson [34] that the decrease in supersaturation from CP is the largest effect during the competition between the two precipitation types.

Despite the variations in microstructures seen with the different cooling rates, all samples had the same hardness within error except the slowest cooled condition, which was around 15% lower. This suggests that solid solution strengthening in the single-phase state is significant, giving similar hardness to alloys with DP and fine CP. However, the coarse CP formed through slow cooling caused softening, likely since solid solution strengthening from Fe is reduced, and the resulting precipitates were too large to provide significant strengthening. Similar age softening due to the removal of solid solution strengthening has been seen in binary Ti-Fe [9]. The formation of the $D8_a$ phase may also have been a contributing factor, but more investigations are needed to confirm this.

4.4. Effect of Mo on B2 precipitation

The effect of Mo content on the competition between the CP and DP mechanisms may rationalise the variation in B2 phase morphology observed with alloy composition. In a study of compositionally simpler Ti-Fe-Mo alloys by Knowles et al. [18], ageing at 750 °C for 80 h produced spherical B2 in Ti-20Fe-10Mo, coarser B2 lamellae in Ti-20Fe-20Mo, and finer lamellae B2 in Ti-20Fe-40Mo. Based on the DP seen in the Ti-Fe-Mo-Al alloys in this work, it is likely that ternary Ti-Fe-Mo alloys are also prone to DP, generating lamellar microstructures. The transition from CP to DP with Mo content in the studied alloys mirrors the transition seen with decreasing temperature in Mg-Al alloys [28]. In the ternary Ti-Fe-Mo system, Mo is the slowest diffuser and has a limited solubility in the B2 phase [12]. As such, for alloys with higher Mo contents, greater Mo diffusion will be required during B2 precipitation. However, higher Mo concentrations will be associated with more sluggish bulk diffusion, which may favour grain boundary diffusion. This would be expected to lead to a transition from CP to DP of the B2 phase. This may explain why Ti-20Fe-10Mo underwent CP when Ti-20Fe-20Mo and Ti-20Fe-40Mo did not, and why coarser lamellae were observed by Knowles in Ti-20Fe-20Mo than Ti-20Fe-40Mo.

This effect of Mo content, together with higher Fe contents increasing the driving force for B2 formation and higher Al contents increasing the driving force for hexagonal A3 and $D0_{19}$ formation, may explain the morphological variations with composition. These variations were most evident in this work after the 600 °C, 1000 h age (Fig. 5). Samples (a) Ti-20Fe-5Mo-5Al and (c) Ti-15Fe-5Mo-10Al have high Fe contents so readily form detectable amounts of B2, and their low Mo contents do not limit the bulk diffusion rate. Thus, they formed CP B2 in conjunction with hexagonal A3 or $D0_{19}$ phases. Sample (b) Ti-15Fe-10Mo-5Al also has a high Fe content, leading to readily detectable B2, but the increased Mo content promoted DP. However, the Mo content was not sufficiently high to fully inhibit CP, so both DP and CP precipitate morphologies were observed. In sample (d) Ti-10Fe-15Mo-5Al a

higher Mo content and low Fe and Al contents limited precipitation. The low Fe and Al concentrations provided only low driving forces for B2 and A3/$D0_{19}$ phase formation, while the increased Mo content limited bulk diffusion. This may account for the low volume fraction of precipitates observed and their restriction to grain boundaries. In (e) Ti-10Fe-10Mo-10Al and (f) Ti-10Fe-5Mo-15Al, the higher Al and lower Fe contents led to little B2 phase formation, and the alloys instead primarily precipitated the A3 or $D0_{19}$ phases.

The complex interplay between alloy composition and heat treatment conditions discussed above highlights the care required when specifying the composition and processing of an alloy based on the Ti-Fe-Mo-Al system. In addition, the disparity between the predicted and observed phases suggests that further studies are warranted to establish the phase equilibria. This would facilitate subsequent studies to develop a structural superlattice precipitate-strengthened alloy based on this system.

5. Conclusions

This work characterised the phases formed following 1000 h isothermal ageing of six alloys derived from the Ti-Fe-Mo-Al quaternary system at three different temperatures, and after controlled cooling of Ti-20Fe-5Mo-5Al. The competition between continuous and discontinuous B2 precipitation mechanisms during controlled cooling and how it influenced microstructural morphology has also been discussed.

From this work, the following conclusions are drawn:

- Isothermal ageing at 1000 °C for 1000 h led to single-phase A2 microstructure in most alloys, with alloy Ti-20Fe-5Mo-5Al having a dual-phase A2+B2 microstructure. Isothermal ageing at 1000 °C for 1000 h generated an A2+B2 microstructure in Ti-20Fe-5Mo-5Al and Ti-15Fe-10Mo-5Al, an A2+B2+$D0_{19}$ microstructure in Ti-15Fe-5Mo-10Al and Ti-10Fe-5Mo-15Al, and a single-phase A2 microstructure was retained in Ti-15Fe-5Mo-10Al and Ti-10Fe-5Mo-15Al. Isothermal ageing at 600 °C for 1000 h caused the A2+B2+A3/$D0_{19}$ phases to be present in the Ti-20Fe-5Mo-5Al and Ti-15Fe-10Mo-5Al, and Ti-10Fe-10Mo-Al alloys. The $D0_{19}$ could be distinctly identified, giving an A2+B2+$D0_{19}$ microstructure, in alloys Ti-15Fe-5Mo-10Al and Ti-10Fe-5Mo-15Al. An A2+A3/$D0_{19}$ microstructure, lacking B2, was observed in alloy Ti-10Fe-5Mo-15Al.
- For the composition Ti-20Fe-5Mo-5Al, fast cooling (40 °C s^{-1}) from the solutioning temperature led to retention of an A2 solid solution. Intermediate cooling (10 to 0.1 °C s^{-1}) led to discontinuous precipitation of B2, with continuous precipitation additionally being observed in a dual-morphology microstructure after 0.1 °C s^{-1} cooling. Slow cooling (0.01 °C s^{-1}) led to fully continuous precipitation. This variation is likely due to a difference in time spent in the temperature regimes where bulk diffusion dominates, causing continuous precipitation, and where grain boundary diffusion dominates, giving rise to discontinuous precipitation.
- Higher concentrations of Mo were shown to be associated with the transition from continuous to discontinuous precipitation. This was attributed to the slow diffusion of Mo and its low solubility in the B2 phase, which affected the relative rates of bulk and grain boundary diffusion.

CRediT authorship contribution statement

A.M.L. Andersson: Formal analysis, Investigation, Methodology, Visualization, Writing – original draft, Writing – review & editing. **R.F.L. Mellor:** Conceptualization, Investigation, Methodology, Writing – review & editing. **J.M. Hogg:** Investigation. **H.C. Cole:** Investigation. **G.I. Lampronti:** Formal analysis. **N.L. Church:** Investigation. **O.S. Houghton:** Investigation. **N.G. Jones:** Conceptualization, Supervision, Writing – review & editing. **H.J. Stone:** Conceptualization, Funding acquisition, Project administration, Supervision, Writing – review & editing.

Funding sources

The authors acknowledge funding from Rolls-Royce, UK and the EPSRC, UK (under grants: EP/V007750/1 and EP/R008779/1), as well as EC H2020 grant 'ESTEEM3' grant agreement ID: 823717.

Research data

The underlying research data required to reproduce these findings are available from the University of Cambridge repository [37].

Declaration of competing interest

The authors declare the following financial interests/personal relationships which may be considered as potential competing interests: H. J. Stone reports financial support was provided by Rolls-Royce plc. R. F. L. Mellor reports financial support was provided by Rolls-Royce plc. H. J. Stone reports a relationship with Rolls-Royce plc that includes: funding grants. If there are other authors, they declare that they have no known competing financial interests or personal relationships that could have appeared to influence the work reported in this paper.

Acknowledgements

The authors thank Dr H.T. Pang for laboratory assistance and useful discussion. Access to the European Synchrotron Radiation Facility was provided under experiment MA5868.

Supplementary information

The online version contains supplementary material also available at http://dx.doi.org/10.17863/CAM.120407 [37].

Data availability

Data will be made available on request.

References

[1] R. Reed, The Superalloys: Fundamentals and Applications, Cambridge University Press, Cambridge, 2006.
[2] T.M. Pollock, S. Tin, Nickel-based superalloys for advanced turbine engines: Chemistry, microstructure, and properties, J. Propuls. Power 22 (2) (2006) 361–374, http://dx.doi.org/10.2514/1.18239.
[3] R.W. Hyland, Homogeneous nucleation kinetics of Al_3Sc in a dilute Al-Sc alloy, Met. Trans. A Phys. Met. Mater. Sci. 23 A (7) (1992) 1947–1955, http://dx.doi.org/10.1007/BF02647542, https://link.springer.com/article/10.1007/BF02647542.
[4] Z. Mao, W. Chen, D.N. Seidman, C. Wolverton, First-principles study of the nucleation and stability of ordered precipitates in ternary Al–Sc–Li alloys, Acta Mater. 59 (8) (2011) 3012–3023, http://dx.doi.org/10.1016/J.ACTAMAT.2011.01.041.
[5] X. Zhao, W. Liu, D. Xiao, Y. Ma, L. Huang, Y. Tang, A critical review: Crystal structure, evolution and interaction mechanism with dislocations of nano precipitates in Al-Li alloys, Mater. Des. 217 (2022) 110629, http://dx.doi.org/10.1016/J.MATDES.2022.110629.
[6] L.A. Cornish, R. Suss, R. Volkl, M. Wederoth, S. Vorberg, B. Fisher, U. Glatzel, A. Douglas, L.H. Chown, T. Murakumo, J. Preussner, D. Lupton, L. Glaner, N. Maledi, J. Potgieter, M. Sphton, G. Williams, Overview of the development of new Pt-based alloys for high temperature application in aggressive environments, J. South Afr. Inst. Min. Met. 107 (11) (2007) 697–711, http://dx.doi.org/10.1007/BF00605003.
[7] J.L. Murray, The Fe-Ti (iron-titanium) system, Bull. Alloy. Phase Diagrams 2 (3) (1981) 320–334, http://dx.doi.org/10.1007/BF02868286, http://link.springer.com/10.1007/BF02868286.
[8] D.V. Louzguine-Luzgin, High-strength ti-based alloys containing Fe as one of the main alloying elements, Mater. Trans. 59 (10) (2018) 1537–1544, http://dx.doi.org/10.2320/matertrans.M2018114.
[9] R. Jones, A. Knowles, W. Clegg, A binary beta titanium superalloy containing ordered-beta tife, alpha and omega, Scr. Mater. 200 (2021) 113905, http://dx.doi.org/10.1016/j.scriptamat.2021.113905, https://linkinghub.elsevier.com/retrieve/pii/S1359646221001858.

[10] J. Das, K.B. Kim, W. Xu, W. Löser, J. Eckert, Formation of ductile ultrafine eutectic structure in Ti–Fe–Sn alloy, Mater. Sci. Eng.: A 449–451 (2007) 737–740, http://dx.doi.org/10.1016/j.msea.2006.02.374, https://linkinghub.elsevier.com/retrieve/pii/S0921509306016662.

[11] A.J. Knowles, N.G. Jones, C.N. Jones, H.J. Stone, Phase equilibria in the Fe-Mo-Ti ternary system at 1173 K (900 °C) and 1023 k (750 °C), Met. Mater. Trans. A: Phys. Met. Mater. Sci. 48 (9) (2017) 4334–4341, http://dx.doi.org/10.1007/s11661-017-4134-6.

[12] A.J. Knowles, N.G. Jones, O.M. Messé, J.S. Barnard, C.N. Jones, H.J. Stone, Phase equilibria in the Fe-Mo-Ti ternary system at 1000 °C, Int. J. Refract. Met. Hard Mater. 60 (2016) 160–168, http://dx.doi.org/10.1016/j.ijrmhm.2016.07.008.

[13] A. Knowles, N. Jones, C. Jones, H. Stone, Phase equilibria and properties of Ti-Fe-Mo alloys with ultra-fine lamellar microstructures, in: Proceedings of the 13th World Conference on Titanium, Wiley, 2016, pp. 1229–1236, http://dx.doi.org/10.1002/9781119296126.ch209, https://onlinelibrary.wiley.com/doi/10.1002/9781119296126.ch209.

[14] Z.P. Jin, C. Qiu, An experimental study and thermodynamic evaluation of the Fe-Mo-Ti system at 1000 °C, Met. Trans. A 24 (10) (1993) 2137–2144, http://dx.doi.org/10.1007/BF02648587, https://link.springer.com/article/{10}.1007/{BF}02648587.

[15] R.F. Mellor, P. Vacek, N.G. Jones, P.A. Midgley, H.J. Stone, Precipitate nanostructuring that enhances lattice compatibility in a Ti-Fe-Al alloy, Scr. Mater. 232 (2023) 115476, http://dx.doi.org/10.1016/J.SCRIPTAMAT.2023.115476.

[16] M. Palm, J. Lacaze, Assessment of the Al-Fe-Ti system, Intermetallics 14 (10–11) (2006) 1291–1303, http://dx.doi.org/10.1016/j.intermet.2005.11.026.

[17] A. Gorzel, M. Palm, G. Sauthoff, Constitution-based alloy selection for the screening of intermetallic Ti-Al-Fe alloys, Z. Metallkunde/Materials Res. Adv. Tech. 90 (1) (1999) 64–70, http://dx.doi.org/10.1515/ijmr-1999-900112, https://www.degruyter.com/document/doi/10.1515/ijmr-1999-900112/html.

[18] A.J. Knowles, T.S. Jun, A. Bhowmik, N.G. Jones, T.B. Britton, F. Giuliani, H.J. Stone, D. Dye, A new beta titanium alloy system reinforced with superlattice intermetallic precipitates, Scr. Mater. 140 (2017) 71–75, http://dx.doi.org/10.1016/j.scriptamat.2017.06.038.

[19] B. Tang, Y. Chu, M. Zhang, C. Meng, J. Fan, H. Kou, J. Li, The ω phase transformation during the low temperature aging and low rate heating process of metastable β titanium alloys, Mater. Chem. Phys. 239 (2020) 122125, http://dx.doi.org/10.1016/J.MATCHEMPHYS.2019.122125.

[20] R Mellor, The Potential for Superlattice Precipitate Reinforcement in Titanium-Iron Alloys (Ph. D. thesis), University of Cambridge, 2023, http://dx.doi.org/10.17863/CAM.106827, https://www.repository.cam.ac.uk/handle/1810/365589.

[21] J.O. Andersson, T. Helander, L. Höglund, P. Shi, B. Sundman, Thermo-calc & DICTRA, computational tools for materials science, Calphad 26 (2) (2002) 273–312, http://dx.doi.org/10.1016/S0364-5916(02)00037-8.

[22] H.M. Rietveld, A profile refinement method for nuclear and magnetic structures, 2, (2) 1969, pp. 65–71, http://dx.doi.org/10.1107/S0021889869006558, urn:issn:0021-8898, https://journals.iucr.org/paper?a07067, https://journals.iucr.org/j/issues/1969/02/00/a07067/.

[23] M. Palm, G. Inden, N. Thomas, The Fe-A1-Ti system, J. Phase Equilib. 16 (3) (1995) 209–222, http://dx.doi.org/10.1007/BF02667305, https://link.springer.com/article/10.1007/BF02667305.

[24] C. Ghosh, J. Basu, D. Ramachandran, E. Mohandas, Phase separation and ω transformation in binary V-Ti and ternary V-Ti-Cr alloys, Acta Mater. 121 (2016) 310–324, http://dx.doi.org/10.1016/J.ACTAMAT.2016.09.028.

[25] D. De Fontaine, N.E. Paton, J.C. Williams, The omega phase transformation in titanium alloys as an example of displacement controlled reactions, Acta Metall. 19 (11) (1971) 1153–1162, http://dx.doi.org/10.1016/0001-6160(71)90047-2, https://www.sciencedirect.com/science/article/pii/0001616071900472.

[26] G.I. Nosova, N.B. D'yakonova, I.V. Lyasotskii, Metastable phases of electron type in titanium alloys with *3d -metals*, Met. Sci. Heat Treat. 48 (9–10) (2006) 427–432, http://dx.doi.org/10.1007/s11041-006-0111-1, http://link.springer.com/10.1007/s11041-006-0111-1.

[27] P.B. Hirsh, A. Howie, R.B. Nicholson, D.W. Pashley, M.J. Whelan, Electron Microscopy of Thin Crystals, Butterworth & Co. LTD., London, 1965.

[28] D. Duly, J.P. Simon, Y. Brechet, On the competition between continuous and discontinuous precipitations in binary Mg-Al alloys, Acta Met. Mater. 43 (1) (1995) 101–106, http://dx.doi.org/10.1016/0956-7151(95)90266-X.

[29] D. Duly, Y. Brechet, Nucleation mechanism of discontinuous precipitation in Mg-Al alloys and relation with the morphology, Acta Met. Mater. 42 (9) (1994) 3035–3043, http://dx.doi.org/10.1016/0956-7151(94)90400-6.

[30] Q. Dong, A. Howells, D.J. Lloyd, M. Gallerneault, V. Fallah, Effect of solidification cooling rate on kinetics of continuous/discontinuous Al_3(Sc,Zr) precipitation and the subsequent age-hardening response in cold-rolled AlMgSc(Zr) sheets, Mater. Sci. Eng.: A 772 (2020) 138693, http://dx.doi.org/10.1016/J.MSEA.2019.138693.

[31] B. Schulz, F. Theska, T. Leitner, M. Hafok, S. Primig, Discontinuous $\gamma\prime$ nucleation due to boron and carbon segregation in Ni-based superalloys, J. Alloys Compd. 1008 (2024) 176459, http://dx.doi.org/10.1016/J.JALLCOM.2024.176459.

[32] V.V. Atrazhev, S.F. Burlatsky, D.V. Dmitriev, D. Furrer, N.Y. Kuzminyh, I.L. Lomaev, D.L. Novikov, S. Stolz, P. Reynolds, The mechanism of grain boundary serration and fan-type structure formation in Ni-based superalloys, Met. Mater. Trans. A: Phys. Met. Mater. Sci. 51 (7) (2020) 3648–3657, http://dx.doi.org/10.1007/s11661-020-05790-5, https://link.springer.com/article/10.1007/s11661-020-05790-5.

[33] M. Hillert, An improved model for discontinuous precipitation, Acta Metall. 30 (8) (1982) 1689–1696, http://dx.doi.org/10.1016/0001-6160(82)90190-0.

[34] J. Robson, Modeling competitive continuous and discontinuous precipitation, Acta Mater. 61 (20) (2013) 7781–7790, http://dx.doi.org/10.1016/j.actamat.2013.09.017, https://linkinghub.elsevier.com/retrieve/pii/S1359645413007027.

[35] R.A. Fournelle, J.B. Clark, The genesis of the cellular precipitation reaction, Met. Trans. 3 (11) (1972) 2757–2767, http://dx.doi.org/10.1007/BF02652842, https://link.springer.com/article/10.1007/BF02652842.

[36] W.D. Zeng, Y.G. Zhou, Effect of beta flecks on mechanical properties of Ti–10V–2Fe–3Al alloy, Mater. Sci. Eng.: A 260 (1–2) (1999) 203–211, http://dx.doi.org/10.1016/S0921-5093(98)00954-X.

[37] A.M.L. Andersson, R.F.L. Mellor, J.M. Hogg, H.C. Cole, G.I. Lampronti, N. Church, O.S. Houghton, N.G. Jones, H.J. Stone, Research Data Supporting "Superlattice phase precipitation in Ti-Fe-Mo-Al alloys", http://dx.doi.org/10.17863/CAM.120407.